Histological and Finite Element Analysis of Cell Death due to Irreversible Electroporation

G. Long, Ph.D.[1]
G. Bakos, M.S.[1]
P. K. Shires, B.V.Sc., M.S.[1]
L. Gritter, M.S.E.[2]
J. W. Crissman, D.V.M., Ph.D.[3]
J. L. Harris, Ph.D.[1]
J. W. Clymer, Ph.D.[1]*

[1]Ethicon Endo-Surgery, Inc.,
4545 Creek R, Cincinnati OH 45242
[2]Altasim Technologies, 130 East Wilson
Bridge Rd, Columbus OH 43085
[3]Vet Path Services, 6450 Castle Drive,
Mason OH 45040

Irreversible electroporation (IRE) has been shown to be an effective method of killing cells locally. In contrast to radiofrequency ablation, the mechanism by which cells are thought to die via IRE is the creation of pores in cell membranes, without substantial increase in tissue temperature. To determine the degree to which cell death is non-thermal, we evaluated IRE in porcine hepatocytes *in vivo*. Using pulse widths of 10 μs, bursts of 3 kV square-wave pulses were applied through a custom probe to the liver of an anesthetized pig. Affected tissue was evaluated histologically via stainings of hematoxylin & eosin (H&E), nitroblue tetrazolium (NBT) to monitor cell respiration and TUNEL to gauge apoptosis. Temperature was measured during the application of electroporation, and heat transfer was modeled via finite element analysis. Cell death was calculated via Arrhenius kinetics. Four distinct zones were observed within the ring return electrode; heat-fixed tissue, coagulation, necrotic, and viable. The Arrhenius damage integral estimated complete cell death only in the first zone, where the temperature exceeded 70°C, and partial or no cell death in the other zones, where maximum temperature was approximately 45°C. Except for a limited area near the electrode tip, cell death in IRE is predominantly due to a non-thermal mechanism.

Key words: Irreversible electroporation; Ablation; Thermal damage; Finite element modeling.

Introduction

Radiofrequency ablation (RFA) of non-resectable malignant and non-malignant tumors has been shown to be equally effective as surgical resection with acceptable morbidity and mortality rates (1). During an RFA procedure, the tumor is heated directly by conductive currents to a temperature sufficient to cause cell death. Although the effects of supraphysiological temperatures on thermal damage is a rate process dependent on the time course of the heating process, the temperature history, and the mechanical state of stress the target tissue is experiencing (2), most RFA procedures rapidly increase the tissue temperature to a sufficiently high level that makes reaching a target temperature a reliable marker of tissue damage. The pattern of heating is related to the current density in the tissue, which depends on the size and spacing of the electrodes used to apply the current. The most commonly used RFA probe is a monopolar (active) probe and a dispersive electrode to form a complete circuit. The active electrode has a small surface area with respect to the return electrode and produces high current density in the tissue, while the large size of the return electrode assures a current density low enough to not heat the tissue. The frequency of the current is chosen

---

*Corresponding author:
J. W. Clymer, Ph.D.
E-mail: jclymer@its.jnj.com

to be high enough to avoid unwanted stimulation of excitable cells (such as cardiac and muscle) during the application (3). The RF current is simply used as a means to heat the tissue; there is no clinically significant electrical interaction within the tissue.

RFA can be performed percutaneously or with laparoscopic assistance. This can significantly reduce the morbidity associated with surgical resection (4). A disadvantage of RFA is the collateral morbidity associated with some tumors (5). Thermal necrosis is also controlled by a time-temperature-stress relationship, but under conditions of constant stress can be described by the Arrhenius rate equation (6). The Joule heating can be considered a distributed heat source in the tissue and is proportional to the current density, which is related to the electrical conductivity of the tissue. The specific absorption rate (SAR) is the quantity of power absorbed by tissue when exposed to RF current:

$$SAR = \frac{\sigma E^2}{\rho} \qquad [1]$$

where σ is the electrical conductivity, E is the electric field and ρ is the density of the tissue. Therefore a more conductive tissue (such as blood) can be a greater source of heat within the tissue. But, the increase of temperature in the tissue due to this heating is determined by the conductive heat equation; thermal conductivity, blood perfusion and fluid flow in a vessel (blood or bile) will each affect the temperature of the tissue. Therefore there is selective heating of the tissue; less perfused, highly conductive tissue will heat the most, while tissue surrounding a large artery will heat the least.

While the intent of thermal therapy is to kill tumor cells, extra-cellular proteins will also be heated and can be denatured, leading to permanent damage to the tissue infrastructure including vital structures (blood vessels, nerves, ducts, *etc.*). For example, a tumor which is centrally located in a liver lobe will be near bile ducts. As the tumor is heated, the nearby bile duct will be heated by current flow as well as by heat conducted by nearby tissue at a higher temperature. This may lead to thermal coagulation of periductal tissue, fibroplasia and contracture causing a narrowing of the bile duct and potentially a blockage. In another situation, a tumor that is located at the periphery of the liver lobe, near the transverse colon, may conduct heat to the adjacent colon causing thermal damage which may lead to colonic perforation. Morbidities such as these can only be eliminated by actively cooling the structure (bile duct) or moving the structure (colon) away from the heat source. Cooling by blood flow can also impede the killing of tumor cells near a blood vessel. It has been reported that perivascular tissue (tumor) remains viable near vessels greater than 3 mm diameter after RF therapy (7) due to this "heat sink" effect.

Electroporation of tissue has been studied for over 50 years (8). It is now well known that an exogenous electric field can change the permeability of the cell membrane to molecules, enabling the molecules to flow into the cytoplasm (9), a phenomenon used to enhance the effect of the neoplastic chemotherapeutic agents, bleomycin (10) and cisplatin (11). It is also well known that increasing the electric field *in-situ* can cause irreversible cell damage leading to cell death without substantially raising the temperature of the tissue (12). Recently, it has been suggested that irreversible electroporation (IRE) could be a useful alternative to thermal therapies as a method of tumor ablation (13, 14). An electric field of 637 V/cm dosed repetitively with eight pulses of 100 µs width has been shown to kill healthy rabbit hepatocytes (15). Theoretically, non-thermal IRE has some advantages over thermal therapies, eliminating the aforementioned morbidities and the heat sink effect.

More than a single pulse is required to cause cell death with IRE (16, 17). Increasing the total number of pulses applies more energy to the tissue and will eventually heat it. A characteristic difference between the RFA waveform and the IRE waveform is that RFA is a true alternating current (AC) waveform while IRE is a monophasic waveform. However, both can cause Joule heating from the conduction current. Therefore one should pay attention to the total energy.

In this study we examined histopathological tissue changes induced by short pulse/high voltage irreversible electroporation and determined whether these changes could be explained in terms of finite element modeling of thermal effects alone.

Materials and Methods

Surgical Procedure

The single pig used in this study was handled and maintained in accordance with the requirements of the Animal Welfare Act (9 CFR Parts 1&2) and its amendments. The study was approved by the Ethicon Endo-Surgery Animal Care and Use Committee as conforming to the standards promulgated in the Guide for the Care and Use of Laboratory Animals, 1996 (NRC, ILAR and National Academy Press).

All procedures were performed with the pig under a surgical plane of general anesthesia maintained by isoflurane inhalation after induction with Telazol® and ketamine. During anesthesia, the animal was continuously monitored for temperature, pulse, respiration, cardiac rhythm and ECG wave form, and circulating oxygen blood levels.

The pig was subjected to liver ablations through a laparotomy. Multiple applications were made directly into the liver with a custom probe (Figure 1). The electrodes were made from stainless steel; the inner needle was sharpened hypodermic tubing with an outer diameter of 1 mm. A 20° bevel was cut on the distal end of the electrode to decrease the penetration force into the liver. The outer ground ring had a diameter of 5 cm and rested on the surface of the liver. A ring electrode was used to fix a relationship that generated radially symmetric and predictable field lines for modeling purposes. This configuration differs from what is used in clinical practice, where two electrodes are utilized in target tissue, since the tissue damage adjacent to the ring electrode is not desirable. The experiment was performed in an open surgery setting, with the liver exposed. The custom fixture with ring electrode was held directly on the naturally moist surface of the liver with light pressure to assure electrode contact.

Two fiber optic temperature sensors (Fiso Technologies, Quebec, QC, Canada) were used to measure the tissue temperature. The first was placed at the distal tip of the needle electrode, the second 1 cm peripheral to the center electrode and 1 cm deep into the tissue.

The generator produces a series of square wave pulses sent in bursts. The total number of pulses per burst and the delay time between each burst determine the average power of the entire dose over time. The total number of bursts determines the total energy. Varying these parameters allowed us to study their effect on the total kill zone and the pathway of cell death.
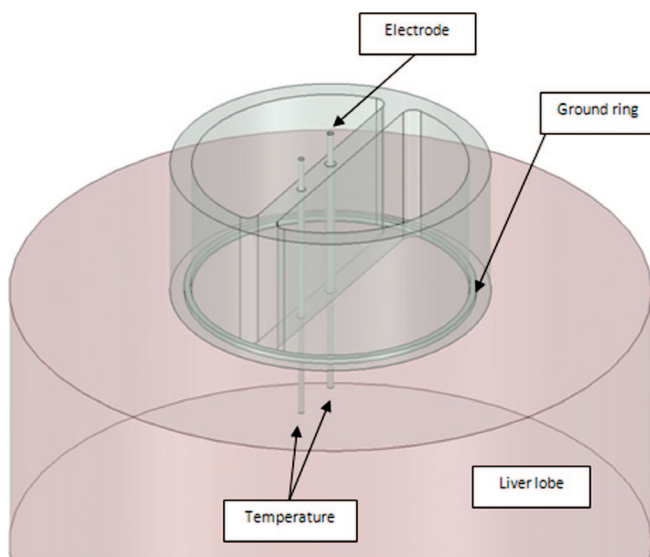
Figure 1: The experimental device used to apply the electrical pulses in the liver lobes. Each needle electrode has a diameter of 1 mm and has insulation beginning 1 cm from the distal tip. The electrode was inserted 1.5 cm into the liver tissue. The temperature was measured and recorded at the end of the positive electrode and at a location 1 cm distal to the positive electrode.

The settings for both the model and experiment were the same. Monophasic square wave pulses with amplitude 3 kV and 10 µs pulse width were delivered. The dose consisted of a total of 300 pulses, grouped into 20 bursts, each containing of 15 pulses. Within each burst, the 15 pulses were delivered with a frequency of 200 Hz. There were 5 seconds delay between the end of one burst and the beginning of the next burst.

The pig was maintained under anesthesia for six hours after treatment, and then euthanized. Multiple previous studies have been performed in our laboratory using pigs to document the percentage cell death and the lesion size at various time points after IRE ablation in the liver. It was determined from these that the six hours interval consistently produces a lesion with the same size as is seen at 24 hours. The percentage cell death within the lesion is in the 85-90% range at 6 hours and 93-98% at 24 hours. For the purposes of this study it was decided that marginal value would be accomplished by recovering the animal from anesthesia in order to obtain 24 hours samples, therefore anesthesia was maintained for 6 hours before the animal was euthanized, thus providing the most humane method of gathering the data. The liver was removed and ablation sites were identified and collected for histopathological analysis. Each ablation was removed as a cylinder of tissue with the central electrode axis perpendicular to the liver surface, and a diameter greater than the ground ring electrode. The cylinder was sectioned parallel to the liver surface at 5 and 10 mm depths. The superficial segment was flash frozen in liquid nitrogen and stored at −200°C for vital staining using nitroblue tetrazolium (NBT). The deeper segment was immersed in triphenyltetrazolium chloride (TTC) for 60 minutes, and then transferred to 10% buffered formalin for 12 hours. At that time the 5 mm deep cut surface was photographed and the specimen returned to buffered formalin until sections were processed and stained with H&E or terminal deoxynucleotidyl transferase dUTP nick end labeling (TUNEL) stains. Tissue morphology was described primarily from the H&E sections, while TUNEL stained sections were used to identify the extent of apoptosis.

The frozen and fixed liver samples were transferred to Premier Laboratory, LLC (Longmont, CO 80504) for histology processing. A set of three large-format (2 × 3 inch) slides was made for each of the four liver lesions created by the procedure. The formalin fixed tissues were stained with either H&E or TUNEL. Cell nuclei with DNA fragmentation stain red with TUNEL, which is believed to be a sensitive indicator of apoptosis. Sections made from the frozen samples were stained for NADH using the NBT stain. Cell respiration produces NADH, thus the NBT stain detects living cells and stains them dark blue. Stained slides were transferred from Premier Laboratory, LLC to Vet Path Services, Inc. (VPS, Mason, OH) for evaluation by a board certified pathologist, James W. Crissman, D.V.M., Ph.D., Diplomate, A.C.V.P.

Finite Element Modeling

Finite element modeling (FEM) is an excellent tool to aid in understanding how the variables affect the outcome. FEM has been applied to RFA (18, 19), as well as with IRE (12, 20, 21). The model uses theory to calculate tissue temperatures and voltage thresholds as a result of certain settings and geometry. The histology photographs demonstrate the experimental results of the same settings. Matching the FEM to the experimental results allows us to understand what type of damage resulted from the voltage threshold and thermal history at particular points within each zone. We modeled and analyzed the application in liver as shown in Figure 1. The liver was modeled as a three dimensional homogeneous mass of tissue. Although attempts have been made to model at a cellular level (22, 23), our interest was in the histology at a macro level. At this scale reasonably accurate results have been achieved (18).

Modeling a homogenous section of liver allowed us to use symmetry and reduce computation time, therefore one quarter of the model was analyzed. The boundary conditions were set as thermal insulation, implying that heat loss was negligible. The temperature at the boundary did increase slightly near the electrode, but in the outer zones the increase was only a few degrees. We examined the tissue deeper in the surface and therefore to reduce computational complexity, we ignored cooling from the surface.

The geometric domains were created using SpaceClaim Engineer (SpaceClaim Corp., Concord MA, USA) and exported to Comsol Multiphysics (Comsol, Inc., Burlington MA, USA) for the analysis. To determine the distribution of the electric field the Laplace equation was solved.

$$\nabla^2 V = 0 \qquad [2]$$

The Pennes bioheat equation was solved to calculate the temperature distribution in the tissue:

$$\rho C \frac{\partial T}{\partial t} + \nabla \cdot (-k\nabla T) = \rho_b C_b \omega_b (T_b - T) + Q_{met} + Q_{ext} \qquad [3]$$

where ρ is the tissue density (1050 kg/m³), C is the specific heat of tissue (3500 J/kg·K), k is the liver tissue's thermal conductivity (0.556 W/(m·K)), ρ_b is the density of blood (1000 kg/m³), C_b is the specific heat of blood (4180 J/kg·K), ω_b is the blood perfusion rate (1.0 × 10⁻³ m³/(m³·s)), T_b is the arterial blood temperature (310 K), Q_{met} is the heat source from metabolism (W/m³), and Q_{ext} is the spatial heat source (W/m³). Schutt *et al.* reported that a change in perfusion due to thermal damage of microvasculature must be incorporated in computational models (24). We have observed vascular necrosis, thrombosis, and inflammation in the central

treatment zone after the first few pulses. Although we did not measure change in perfusion, we reduced the value of ω_b as a functional parameter from the value typically reported (6.4 × 10⁻³ m³/(m³·s)) (19) until the experimental temperature plot aligned well with the model temperature plot.

The product of the electric field and the current density was used as the spatial heat source (Joule heating) and the heating due to metabolism was considered insignificant because our calculations showed that the heating due to the applied field was 9 orders of magnitude greater than values reported in the literature (25), therefore Equation [3] becomes:

$$\rho C \frac{\partial T}{\partial t} + \nabla \cdot (-k\nabla T) = \rho_b C_b \omega_b (T_b - T) + J \cdot E \qquad [4]$$

where J is the current density (A/m²), and E is the electric field (V/m).

The current flow in biological tissue is proportional to the electrical conductivity, which is a function of temperature (19, 25) and is modeled as:

$$\sigma(T) = \sigma_0 \left[1 + \alpha(T - T_0) \right] \qquad [5]$$

where for liver tissue $\sigma_0 = 0.2\,\mathrm{S}^{-1}$ and $\alpha = 0.015\,\mathrm{T}^{-1}$. As the tissue is heated, the conductivity will change which will affect the distribution of the heat source within the tissue. Electroporation will itself also affect the conductivity. Furthermore, the value of the electric field at each point will change as the conductivity changes to satisfy the Laplace equation. The current density will have the highest value near the electrodes which will be where the tissue will heat the greatest. The settings for the application that was modeled were 3 kV, 10 μs pulse width, 15 pulses per burst, 200 Hz pulse rate, 20 bursts and a 5 seconds delay between each burst. The electrical parameters chosen reflect a practical aggregation of factors that influence speed of delivery, size of lesion, tissue temperature and host reactions. At the chosen parameters, muscle contractions were minimal and did not require synchronization of the pulses with heart beat.

Arrhenius Damage Model

The damage caused by heating the tissue is estimated by the Arrhenius rate equation which describes the temperature dependency of chemical reactions (26-28):

$$\frac{dn}{dt} = -nAe^{\frac{-\Delta E}{RT}} \qquad [6]$$

where n is the number of cells that have not died, R is the universal gas constant, T is the temperature in Kelvin and A ($7.39 \times 10^{39} \, \text{s}^{-1}$) and ΔE ($2.58 \times 10^{5} \, \text{J/mol}$) are the reaction parameters (29).

The solution is:

$$\frac{n(\tau)}{n0} = e^{-\Omega(\tau)} \qquad [7]$$

where:

$$\Omega(\tau) = A \int_{t=0}^{\tau} e^{\frac{-\Delta E}{\text{RT}(t)}} dt \qquad [8]$$

The damage integral was calculated by trapezoidal integration of Equation 8, using temperatures at timepoints provided by the model. A value of $\Omega = 1$ has been reported as the point at which thermal damage begins and $\Omega = 4.6$ is the value where thermal damage is complete (8).

Results

Histopathology

Circular lesions, each with tissue effects in a concentric zoned pattern were examined. Figures 2A, 2B, and 2C show the overall zonation of effects as observed by low magnification scans of the three stains employed in this study. The NBT stain for NADH (Figure 2C) was negative in zones 1 and 2, weakly positive in zone 3, strongly positive in zone 4, and weakly positive or negative in zone 5 under the ring electrode. The TUNEL stain for fragmented DNA (Figure 2B) was mostly negative in zones 1 and 2, but strongly positive in zone 3, the hemorrhagic zone. TUNEL staining was mostly negative or showed scattered small patches of positivity in zone 4, and finally there were scattered positively staining individual cells under the ring electrode in zone 5. The descriptions below represent the zones in order, from the central penetrating electrode to the outer ring electrode observed from the H&E stained sections (Figure 2A).

Zone 1, the area immediately surrounding the central electrode, was the central zone of tissue destruction and was one to two liver lobules in diameter. In this zone there was loss of tissue architecture, and extensive hemorrhage. Hepatocyte ghosts could be identified in H&E sections; parenchymal areas showed only pale pink outlines of cell membranes with even paler cell contents. A medium sized artery on the periphery of this zone showed hemorrhage and necrosis in the

vessel wall, with early thrombus development characterized by laminar accretion of fibrin and erythrocytes. Accompanying veins showed massive accumulations of neutrophils. An accompanying bile duct showed occasional apoptotic cells, but appeared otherwise normal.

The zone of coagulation, zone 2, was one to two lobules thick. In this zone, hepatocyte nuclei appeared pyknotic, *i.e.*, homogenous and dark, with loss of the normal nuclear chromatin pattern. Many erythrocytes had apparently been lysed, and appeared as flocculent pink material or ghosts in sinusoids. Hepatocyte cytoplasm appeared slightly condensed, making the space of Disse appear prominent. Near the outer edge of this region, sinusoids appeared dilated and blood filled.

In zone 3, which was approximately five to six lobules thick, the predominant features were congestion and hemorrhage. There was marked sinusoidal congestion with hemorrhage into the space of Disse. Hepatocyte nuclei appeared slightly pyknotic with some margination of chromatin. Hepatocyte cytoplasm was condensed, often with small clear peripheral vacuoles. The effects were not homogeneous within this zone; mid- and centrilobular areas sometimes appeared more like the central coagulative zone with red cell lysis, while peripheral lobular areas showed more congestion and hemorrhage.

At the outer edge of the hemorrhagic zone 3, some liver lobules showed patchy necrosis, often with distinct zonation of effects in mid- and centrilobular anatomic areas, while at the lobular peripheries, hepatocytes appeared near normal. In the transition zone between clearly necrotic and apparently normal, there was often a zone of hepatocyte nuclear karyorrhexis (fragmentation).

In the next zone, zone 4, there was occasional patchy hepatocyte necrosis, generally in mid-lobular areas. However, most zone 4 hepatocytes appeared normal out to the beginning of zone 5, the area under the ring electrode (where present in section). The area under the electrode ring showed areas of necrosis, with pyknosis, karyorrhexis, and hemorrhage. Where present in the section (rarely), zone 6, the area outside the ring electrode, appeared normal.

The reporting pathologist concluded that there was distinct zonation of observable effects caused by the pulsed electrical field 6 hours after it was applied to the liver of an anesthetized pig.

There were two notable patterns observed. First, at this time period, the killing effect declined with distance from the central electrode, except directly under the outer ring electrode. Second, within zones with substantial but not
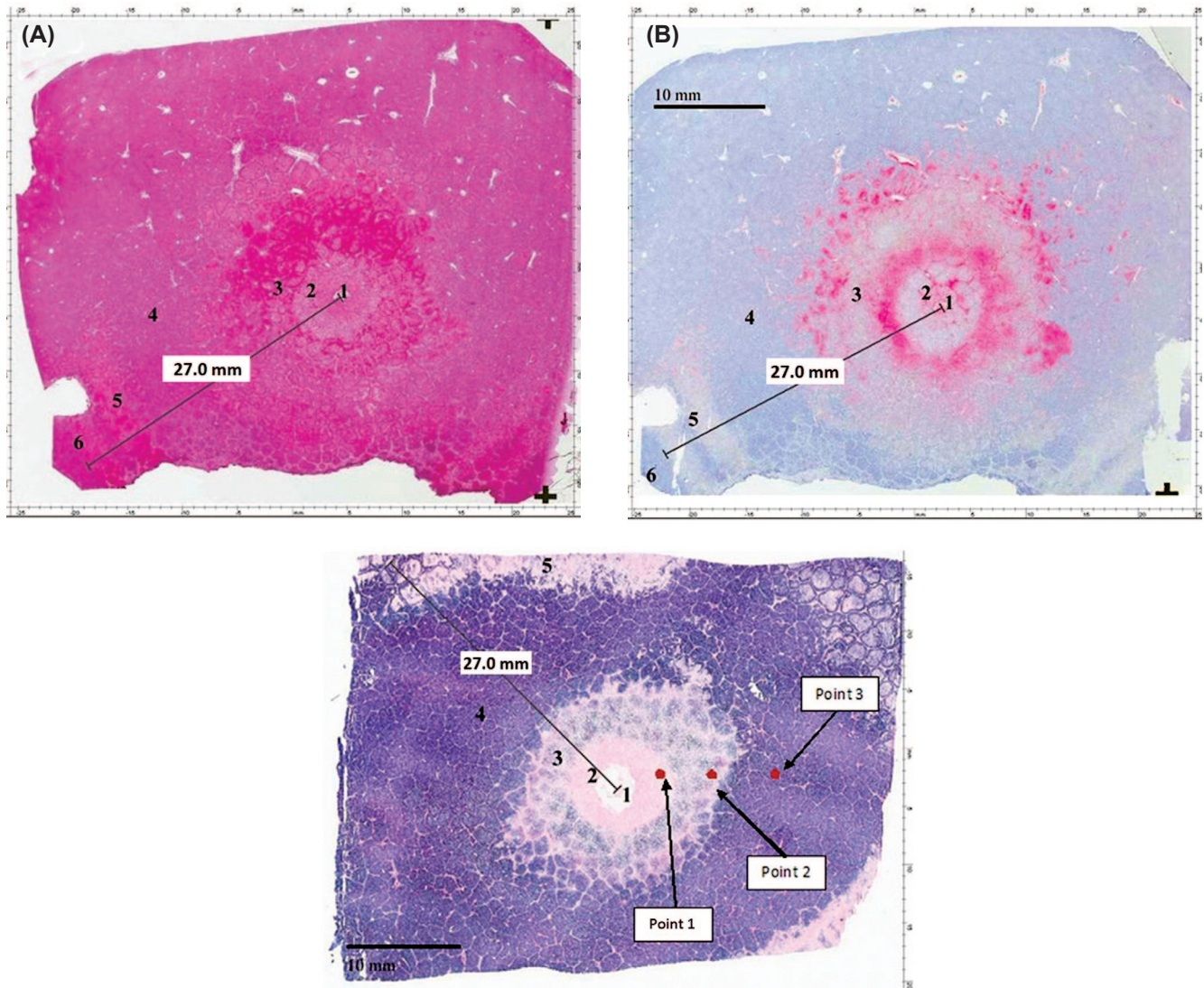
Figure 2: (**A**) H&E, lesion 3. Low magnification scanned image of liver showing numbered zones of the effects of the IRE apparatus. Zone 1 represents the immediate area of the central positive electrode. Zone 5 is the approximate location of the negative ring electrode. Zones 2, 3, and 4 show concentric layers of effect between the 2 electrodes. Zone 6 represents tissue outside the outer ring. Zones 5 and 6 were not present in all sections. (**B**) TUNEL, lesion 3. Low magnification scanned image of same section of liver as Figure 2, showing numbered zones of the effects of the IRE apparatus. Red staining with TUNEL represents concentrations of nuclei undergoing cell death. (**C**) NBT, lesion 2. Low magnification scanned image of liver showing numbered zones of the effects of the IRE apparatus. Blue staining with NBT on frozen tissue indicates cells producing NADH, a marker for living cells. A tissue zone outside the outer ring electrode could not be clearly identified in this section. The three red dots denote the points at which the finite element analysis was performed.

complete tissue destruction, there was often an anatomic pattern to the damage, with the mid-lobular areas apparently being the most sensitive to the effects of IRE, while peripheral lobular areas, and to a lesser extent, centrilobular areas tended to be spared.

Finite Element Modeling

The models were run on an Intel Core i7 CPU at 3.07 GHz with 12.0 GB of RAM. The tetrahedral mesh generated for

each model had 27,277 elements and 61,164 degrees of freedom. The solution time was 11 hours.

Figure 3 is a plot of the experimental temperature compared with the temperature predicted by the model for the electrode and the 1 cm location.

Figure 4 is a plot of the percentage of dead cells, derived from Ω, the damage integral, calculated from Arrhenius kinetics as a function of time for the points at which the electrode
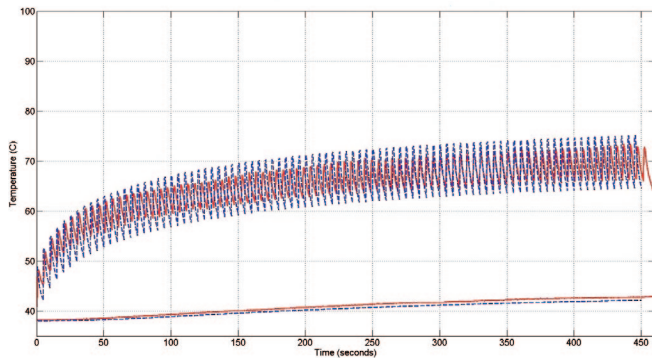
Figure 3: Plot of the experimental (red) and model (blue) temperatures at the electrode (upper pair of traces) and 1 cm away (lower pair).
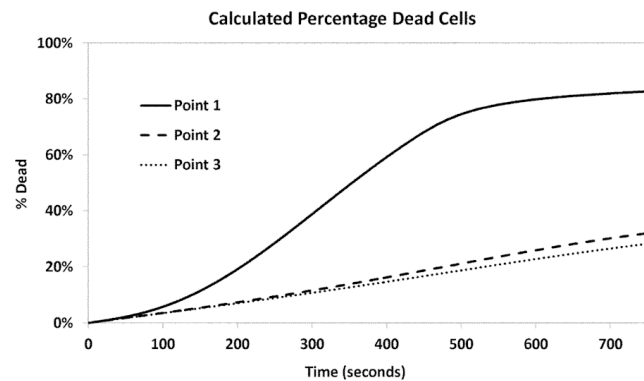
Figure 4: Percentage of dead cells calculated from the Arrhenius damage integral at the points identified in Figure 4. The damage is that calculated from thermal exposure and does not include direct electroporation effects.

and 1 cm temperatures were recorded. A point in each zones 1, 2 and 3 were analyzed (red dots in Figure 2C). The accumulated damage in zone 1 shows thermal damage ($\Omega = 4.6$ at 70 seconds) while zones 2 and three do not (zone 2 max $\Omega = 0.2$ and zone 3 max $\Omega = 0.03$). Cell death continues until the temperature decreases, which occurs sometime after pulses are stopped. Apoptosis is one avenue of cell death observed, and this is progressive over at least 18 to 24 hours after IRE ablation.

The results of the histological analysis and finite element modeling are summarized in Table I.

Discussion and Conclusion

We intentionally created a lesion which contains thermal damage as well as cell death due to IRE. The experimental plot in Figure 4 shows that the tissue at the electrode was damaged thermally while the tissue at the 1 cm location did not reach a time-temperature-load combination sufficient to cause thermal damage (yet cells were dead at the 1 cm location). The temperature at the central electrode reached a point where the tissue was heat-fixed (Zone 1). Immediately surrounding that was a zone of coagulation which suggests protein denaturation results from the time-temperature-load conditions during treatment (Zone 2). Intra-vascular thrombosis was found within these 2 zones, compounding the tissue damage resultant from electrical field changes.

The clinical impact of this relates to how the body resolves the damage. Heat fixed or coagulated protein is treated as a sterile foreign body which must be isolated by the innate immune system and slowly digested by enzymatic action. The accumulation of white blood cells in veins within and around these zones attests to the beginning of that response. The lack of TUNEL staining in these two zones is an indicator that the cell death pathway did not include apoptosis. The outer edge of zone 2 does begin to show blood-filled sinusoids which are probably the transition to hemorrhage seen in the next zone.

Zone 3 shows little indication of thermal injury. Hemorrhage, nuclear pyknosis, and intra-cellular vacuolation appear have a patchy distribution. Toward the outer edge of this zone the liver architecture seems to be influencing the patchy distribution. Within each liver lobule the center was abnormal while the periphery not obviously so. In between these was a layer of nuclear fragmentation.

Since we know from 24 hours survival studies that complete cell death takes more than the 6 hours observed here, we could be observing the distribution pattern of cells on their way to death in this zone. This is supported by the high incidence of TUNEL stained nuclei indicating an apoptotic pathway of cell death. Speculation about why some

Table I
Summary of stain results for the various zones around the electrode.

| Zones	Approx. diameter (mm)	Post-IRE condition	H&E (structure)	NBT (vitality)	TUNEL (apoptosis)	Maximum temperature (°C)	Ω
1	10	Heat-fixed tissue	Ghosts, neutrophils	−	−	72	>4.6
2	25	Coagulation	Pyknotic	−	−	45	0.2
3	40	Necrotic	Congestion, hemorrhage	+	++	39	0.03
4	50	Viable	Normal	++	−/+	38	<0.01
5	53	Under ring electrode	Pyknosis, hemorrhage	+/−	−/+	Not measured	Not calc.

hepatocytes might be more resistant to apoptosis induced by the electrical field effects should include the fact that blood reaching the centrilobular region of the liver is oxygen-depleted.

Zone 4 is outside of the area that cells uniformly die. The occasional focus of cell death in this zone begs the question as to the uniformity of electrical field distribution. There appear to be some "less vulnerable" spots within zone 3, and some "more sensitive" spots within zone 4. There is probably some unidentified pathway(s) of least electrical resistance through the tissue, a possibility supported by the widely variable degree of injury immediately under the negative ring electrode (zone 5).

The all-or-nothing phenomenon of protein coagulation or heat fixation is not characteristic of the electrical field tissue changes. The factors that determine the cell death pathway to be lytic, apoptotic, or delayed lysis are not clearly differentiated by anatomy or proximity to the positive electrode. There is clearly an electrical field strength level below which cell death is not induced, but whether the fine discrimination of cell death pathway and timing is purely by electrical field strength, or a combination of field strength and local factors like oxygenation, age of cell, nutritional status or stage of replication is not apparent. This study is a picture of one moment in the 18-24 hours process of complete expression of the effects of a pulsed electrical field.

While the critical cell death electric field threshold of 637 V/cm has been reported for a pulse width of 100 μs and 8 pulses, we have observed an IRE threshold in the range of 800 V/cm to 900 V/cm for a 10 μs pulse width. This pulse width is closer to the typical cell membrane charging time in mammals on the order of 100 ns, at which width the membrane is affected. Furthermore, at low average powers, thermal effects should not occur (30, 31). Figure 5 is the NADH stained slide with the predicted location of 800 V/cm to 900 V/cm as well as a 450 V/cm to 500 V/cm ranges. This increase in threshold may be due to changes in conductivity following electroporation, which will modify the electric field distribution in the vicinity of the electrode. We also believe that the change in the threshold may be related to tissue heating. The temperature-dependent electrical conductivity will shift the electric field as the tissue is heated. Benz *et al.* reported a temperature dependency of the membrane breakdown voltage (32). The higher threshold is located 2.1 cm from the center. The predicted temperature at the end of the treatment for that location is 45°C.

Limitations of this study include the fact that only a single pig was used for multiple applications. To demonstrate repeatability, additional studies should be performed with more than one animal.
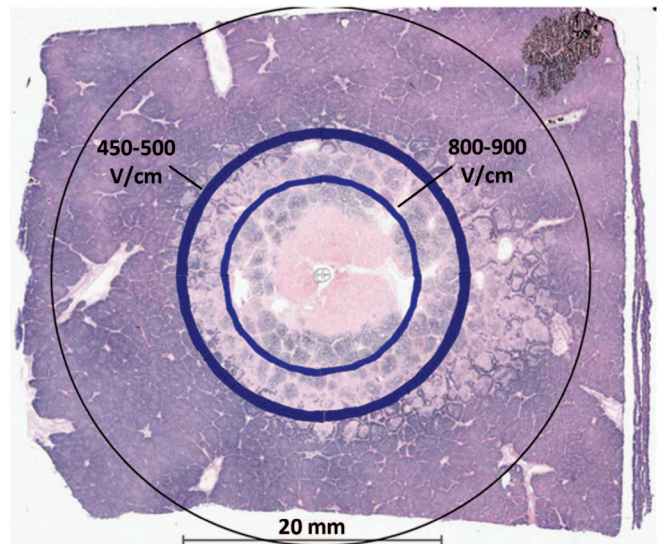
Figure 5: Overlay of two ranges of the predicted electric field range. The necrotic edge was expected to be in the 800 V/cm to 900 V/cm range. The actual necrotic edge aligns with a range of 450 V/cm to 500 V/cm. The discontinuities are due to the use of symmetry; the electric field solution was copied and rotated to create a complete diameter. The outer circle represents the ground ring electrode.

We have not attempted to take into account the increase of tissue conductivity due to electroporation in our modeling. While we have observed a change of electrical conductivity as a function of electric field strength, since we are calculating the current by integrating the current density over the electrode surface, we cannot account for the transient changes in the conductivity due to the intense electric field. Our experience has taught us that the changes in electrical conductivity due to temperature changes are much greater.

During IRE a substantial increase in temperature accompanied by thermal cell death only occurs within a limited region around the electrodes. Outside this small region, the temperature is minimal, and death occurs by a non-thermal cell membrane poration mechanism.

Conflict of Interests

We certify that regarding this paper, no actual or potential conflict of interests exist; the work is original, has not been accepted for publication nor is concurrently under consideration elsewhere, and will not be published elsewhere without the permission of the Editor and that all the authors have contributed directly to the planning, execution or analysis of the work reported or to the writing of the paper.

References

1. Berber E & Siperstein AE. Perioperative outcome after laparoscopic radiofrequency ablation of liver tumors: an analysis of 521 cases. *Surg Endosc 21*, 613-618 (2007). DOI: 10.1007/s00464-006-9139-y

2. Humphrey JD. Continuum thermomechanics and the clinical treatment of disease and injury. *Applied Mechanics Review 56*, 231-260 (2003). DOI: 10.1115/1.1536177

3. LaCourse JR, Vogt MC, Miller III, WT & Selikowitz SM. Spectral analysis interpretation of electrosurgical generator nerve and muscle stimulation. *IEEE Trans Biomed Eng 35*, 505-509 (1988). DOI: 10.1109/10.4578

4. Decadt B & Siriwardena AK. Radiofrequency ablation of liver tumours: systematic review. *Lancet Oncol 5*, 550-560 (2004). DOI: 10.1016/S1470-2045(04)01567-0

5. Gillams AR. Complications of percutaneous therapy. *Cancer Imaging 5*, 110-113 (2005).

6. Henriques FC. Studies of thermal injuries V. The prediction and significance of thermally-induced rate processes leading to irreversible epidermal injury. *Arch Pathol 43*, 489-502 (1947).

7. Lu DS, Raman SS, Vodopich DJ, Wang M, Sayre J & Lassman C. Effect of vessel size on creation of hepatic radiofrequency lesions in pigs: assessment of the "heat sink" effect." *Am J Roentgenol 178*, 47-51 (2002).

8. Stamplfi R. Reversible electrical breakdown of excitable membrane of a Ranvier node. *Ann Acad Brasil Ciens 30*, 57-63 (1958).

9. Weaver JC & Chizmadzhev Y. Theory of electroporation: A review. *Bioelectrochemistry Bioenergetics 41*, 135-160 (1996). DOI: 10.1016/S0302-4598(96)05062-3

10. Mir LM, Orlowski S, Belehradek J, Jr & Paoletti C. Electrochemotherapy potentiation of antitumour effect of bleomycin by local electric pulses. *Eur J Cancer 27*, 68-72 (1991). 10.1016/0277-5379-(91)90064-K

11. Sersa G, Cemazar M & Miklavcic D. Antitumor effectiveness of electrochemotherapy with cis-diamminedichloroplatinum(II) in mice. *Cancer Res 55*, 3450-3455 (1995).

12. Rubinsky B. Irreversible electroporation in medicine. *Technol Cancer Res Treat 6*, 255-260 (2007).

13. Miller L, Leor J & Rubinsky B. Cancer cells ablation with irreversible electroporation. *Technol Cancer Res Treat 4*, 699-705 (2005).

14. Zupanic A, Kos B & Miklavcic D. Treatment planning of electroporation-based medical interventions: electrochemotherapy, gene electrotransfer and irreversible electroporation. *Phys Med Biol 57*, 5425-5440 (2012). DOI: 10.1088/0031-9155/57/17/5425

15. Miklavcic D, Semrov D, Mekid H & Mir LM. A validated model of in vivo electric field distribution in tissues for electrochemotherapy and for DNA electrotransfer for gene therapy. *Biochim Biophys Acta 1523*, 73-83 (2000). DOI: 10.1016/S0304-4165(00)00101-X

16. Edd JF, Horowitz L, Davalos RV, Mir LM & Rubinsky B. In vivo results of a new focal tissue ablation technique: irreversible electroporation. *IEEE Trans Biomed Eng 53*, 1409-1415 (2006). DOI: 10.1109/TBME.2006.873745

17. Pavselj N, Bregar Z, Cukjati D, Batiuskaite D, Mir LM & Miklavcic D. The course of tissue permeabilization studied on a mathematical model of a subcutaneous tumor in small animals.

IEEE Trans Biomed Eng 52, 1373-1381 (2005). DOI: 10.1109/TBME.2005.851524

18. Chang IA & Nguyen UD. Thermal modeling of lesion growth with radiofrequency ablation devices. *Biomed Eng Online 3*, 27 (2004). DOI: 10.1186/1475-925X-3-27

19. Chang IA. Finite element analysis of hepatic radiofrequency ablation probes using temperature-dependent electrical conductivity. *Biomed Eng Online 2*, 12 (2003). DOI: 10.1186/1475-925X-2-12

20. Davalos RV, Mir IL & Rubinsky B. Tissue ablation with irreversible electroporation. *Ann Biomed Eng 33*, 223-231 (2005). DOI: 10.1007/s10439-005-8981-8

21. Pavselj N & Miklavcic D. Numerical modeling in electroporation-based biomedical applications. *Radiol Oncol 42,* 159-168 (2007). DOI: 10.2478/v10019-008-0008-2

22. Gowrishankar TR & Weaver JC. An approach to electrical modeling of single and multiple cells. *Proc Natl Acad Sci USA 100*, 3203-8 (2003). DOI: 10.1073/pnas.0636434100

23. Essone Mezeme M, Pucihar G, Pavlin M, Brosseau C & Miklavcic D A numerical analysis of multicellular environment for modeling tissue electroporation. *Applied Physics Letters 100*, 143701 (2012). DOI: 10.1063/1.3700727

24. Schutt DJ & Haemmerich D. Effects of variation in perfusion rates and of perfusion models in computational models of radio frequency tumor ablation. *Med Phys 35*, 3462-3470 (2008). DOI: 10.1118/1.2948388

25. Lackovic I, Magjarevic R & Miklavcic D. Three-dimensional finite-element analysis of Joule heating in electrochemotherapy and in vivo gene electrotransfer. *IEEE Trans Dielectrics Electrical Insulation 16*, 1338-1347 (2009). DOI: 10.1109/TDEI.2009.5293947

26. Pearce JA. Relationship between Arrhenius models of thermal damage and the CEM 43 thermal dose. *Energy-based Treatment of Tissue and Assessment V, Proc SPIE 7181*, 1-15 (2009). DOI: 10.1117/12.807999

27. Chang IA. Considerations for thermal injury analysis for RF ablation devices. *Open Biomed Eng J 4*, 3-12 (2010).

28. Shafiee H, Garcia PA & Davalos RV. A preliminary study to delineate irreversible electroporation from thermal damage using the Arrhenius equation. *J Biomech Eng 131*, 074509 (2009). DOI: 10.1115/1.3143027

29. Humphries S. Arrhenius rate integrals in computer thermal solutions. *Field Precision 5* (2008).

30. Joshi RP & Schoenbach KH. Bioelectric effects of intense ultrashort pulses. *Crit Rev Biomed Eng 38*, 255-304 (2010).

31. Schoenbach KH, Hargrave B, Joshi RP, Kolb JF, Nuccitelli R, Osgood C, Pakhomov A, Stacey M, Swanson RJ, White JA, Xiao S, Zhang J, Beebe SJ, Blackmore PF & Buescher ES. Bioelectric Effects of Intense Nanosecond Pulses. *IEEE Trans on Dielectric Electrical Insulation 14*, 1088-1109 (2007). DOI: 10.1109/TDEI.2007.4339468

32. Benz R, Beckers F & Zimmermann U. Reversible electrical breakdown of lipid bilayer membranes: a charge-pulse relaxation study. *J Membr Biol 48*, 181-204 (1979).